

Article

Hard Carbons Derived from Phenyl Hyper-Crosslinked Polymers for Lithium-Ion Batteries

Ziyang Guo ^{1,2}, Xiaodong Tian ³ , Yan Song ^{3,4,*}, Tao Yang ³, Zihui Ma ^{3,4}, Xiangjie Gong ^{3,4} and Chao Wang ^{1,2,*}¹ College of Materials Science and Engineering, North University of China, Taiyuan 030051, China² Advance Energy Materials and Systems Institute, North University of China, Taiyuan 264000, China³ CAS Key Laboratory for Carbon Materials, Institute of Coal Chemistry, Chinese Academy of Sciences, Taiyuan 030001, China⁴ Center of Materials Science and Optoelectronics Engineering, University of Chinese Academy of Sciences, Beijing 100049, China

* Correspondence: yansong1026@126.com (Y.S.); wangchao_nuc@126.com (C.W.); Tel.: +86-351-2021135 (Y.S.)

Abstract: Hyper-crosslinked polymers are attracting extensive attention owing to their ease of design and synthesis. Based on the flexibility of its molecular design, a hyper-crosslinked polymer with a π -conjugated structure and its derived carbon were synthesized by the Friedel–Crafts reaction. The polymer and its derived hard carbon material were characterized by FTIR, ¹³C NMR, Raman, BET, and other characterization tools. The electrochemical properties of both materials as anode electrodes of lithium-ion batteries were investigated. Benefiting from the highly cross-linked skeleton and conjugated structure, the as-prepared carbon materials still had high specific surface area (583 m² g⁻¹) and porosity (0.378 cm³ g⁻¹) values. The hard carbon (CHCPB) anode possessed the powerful reversible capacity of 699 mAh g⁻¹ at 0.1A g⁻¹, and it had an excellent rate of performance of 165 mAh g⁻¹ at the large current density of 5.0 A g⁻¹. Long-cycle performance for 2000 charge/discharge cycles displayed that the capacity was kept at 148 mAh g⁻¹ under 2 A g⁻¹. This work contributes to a better understanding of the properties of hard carbon materials derived from hyper-crosslinked polymers and how this class of materials can be further exploited in various applications.



Citation: Guo, Z.; Tian, X.; Song, Y.; Yang, T.; Ma, Z.; Gong, X.; Wang, C. Hard Carbons Derived from Phenyl Hyper-Crosslinked Polymers for Lithium-Ion Batteries. *Coatings* **2023**, *13*, 421. <https://doi.org/10.3390/coatings13020421>

Academic Editor: Octavian Buiu

Received: 2 December 2022

Revised: 9 February 2023

Accepted: 10 February 2023

Published: 13 February 2023



Copyright: © 2023 by the authors. Licensee MDPI, Basel, Switzerland. This article is an open access article distributed under the terms and conditions of the Creative Commons Attribution (CC BY) license (<https://creativecommons.org/licenses/by/4.0/>).

Keywords: hyper-crosslinked polymers; π -conjugated; hard carbon; anode materials; lithium-ion batteries

1. Introduction

Lithium-ion batteries (LIBs) are widely used as smart portable electronic devices and powered vehicles because of their high energy/power density and long cycle life [1–3]. As a key component of LIBs, the anode material plays an important role in improving the overall performance. Graphite, a commercial anode material, cannot meet the increasing demand of energy and power density due to its limited theoretical capacity (372 mAh g⁻¹) and poor rate performance [4–6]. Therefore, it is challenging to develop next-generation advanced anode materials with high reversible capacity, excellent rate performance, and long cycle life.

Hard carbon is the preferred anode material compared with graphite and soft carbon due to its short-range graphitization domains, rich pores, and abundant edges and defects. The unique structures facilitate the transport of Li⁺ ions and provide them with abundant active sites [7,8]. According to research, nanotextures and synthesis conditions of the precursors can modulate the microstructures of the obtained hard carbon and thus affect its electrochemical performance [9–12]. There are various precursor substances of the preparation of hard carbon, such as coal tar pitch (CTP), biomass, resin, and polymer [13–15]. Fujimoto et al. prepared hard carbon with different oxygen contents under three different pretreatment conditions using CTP as the precursor [13]. Fromm et al. prepared hard carbon from bamboo precursors to investigate the effect of heat treatment temperatures on the

microstructure and electrochemical properties of the as-obtained hard carbon [14]. Gao and co-workers successfully prepared resin-based hard carbon by pyrolyzing and carbonizing the phenolic resin precursor at 1100 °C [15]. However, there will be an inevitable limitation for CTP produced from fossil resources for future applications from the perspective of sustainable development. The heterogeneity of biomass composition, the high cost of resin, and the low carbon yield all limit their use as the promising precursors for hard carbon materials.

Hyper-crosslinked polymers (HCPs), synthesized by the Friedel–Crafts reaction [16], can provide a more ideal method for hard carbon owing to the characteristics of extensive monomers resources and high carbon yield. Noteworthy, the framework structure and the surface properties of HCPs are flexible and adjustable, which can be modified by changing the geometric shape of the monomer, the type of functional group and chain length of crosslinker, or by doping hetero atoms. This means that high performance carbon electrode materials with oriented structure are expected to be made by rational design and preparation. Recent research has shown that HCP-derived carbon materials by various strategies exhibit great potential in the field of electrochemical energy storage [17–22]. For instance, porous carbon nanotubes (HCPs) with different morphologies and sizes were obtained by adjusting the initial monomer concentration and molecular sizes of HCPs, which were prepared by a self-templated, surfactant-free strategy. The authors found that the obtained PCNTs showed excellent electrochemical performance for supercapacitors [23]. A porous carbon material carbonized from hyper-crosslinked porous polymers gave a specific capacity of 1221 mAh g⁻¹ at 0.1 A g⁻¹ and a satisfactory capacity of supercapacitors [19]. Guan et al. successfully fabricated honeycomblike porous carbons with specific pore structures by adjusting the dosage of chloroform, which showed an ultrahigh surface area of 3473.0 m² g⁻¹ and abundant mesopores with sizes of 2–5 nm [24]. A microporous carbon (MICHP) derived from hyper-crosslinked polystyrene was obtained through a facile molecular crosslinker design strategy, which exhibited a surface area of 387 m² g⁻¹ [25].

The current work profitably synthesizes a hyper-crosslinked polymer (HCP) with a π -conjugated structure by the Friedel–Crafts reaction of benzene and 1,4-dimethoxybenzene (DMB). Then, a hard carbon material with a layer-stacked structure is obtained by high-temperature treatment of the HCP precursor. The hard carbon material inherits the rigid skeleton of the HCP precursor and has a similar specific surface area and pore volume. When employed as an anode of LIBs, it shows a satisfying rate capacity of 699 mAh g⁻¹ at 0.1 A g⁻¹ and 165 mAh g⁻¹ at the large current density of 5.0 A g⁻¹. After cycling 2000 times at 2.0 A g⁻¹, the reversible capacity can reach 148 mAh g⁻¹. This work provides a new promising strategy and fundamental understanding of carbon-based electrodes derived from HCPs for rechargeable batteries.

2. Materials and Methods

2.1. Materials

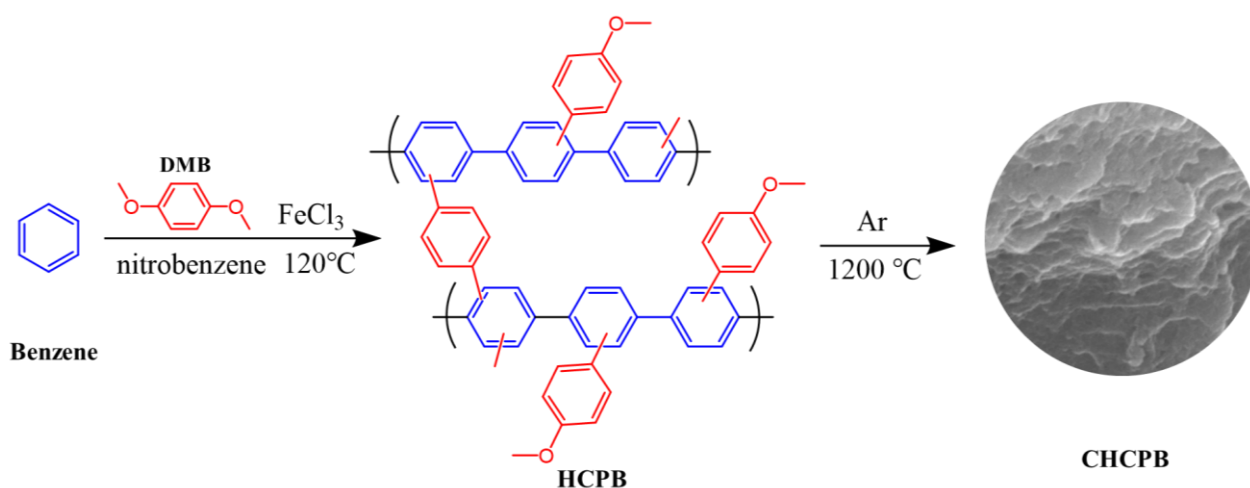
1,4-Dimethoxybenzene (DMB, 99%), nitrobenzene, and FeCl₃ (anhydrous) were purchased from MACKMIN Co., Ltd. (Shanghai, China). Benzene and methanol were purchased from Kermel Co., Ltd. (Tianjin, China). Conductive carbon black, polyvinylidene fluoride (PVDF), and 1 M LiPF₆ in a mixed solvent of vinyl carbonate (EC), and diethyl carbonate (DEC) (1:1, vol/vol) with 5.0% fluoroethylene carbonate (FEC) was obtained from Suzhou DuoDuo Chemical Technology Co., Ltd. (Suzhou, China). The commercial hard carbon (CHC) was obtained from KUREHA Chemical Co., Ltd. (Shanghai, China).

2.2. Synthetic Procedures for Hyper-Crosslinked Polymers and Hard Carbon Materials

Benzene (0.13 g, 1.67 mmol) and DMB (0.69 g, 4.99 mmol) were added into 15 mL of nitrobenzene. Then, anhydrous FeCl₃ (2.44 g, 15.02 mmol) was added to the above-mixed solution at room temperature. After that, the reaction system was stirred for 5 h at 45 °C, 5 h at 80 °C, and 24 h at 120 °C to obtain a porous polymer. After cooling to room

temperature, the crude product was washed with hydrochloric acid and methanol in turn until the filtrate became colorless. Then, the target product was extracted with methanol for 48 h in a Soxhlet extractor and dried under vacuum at 60 °C for 24 h. The final product was named HCPB.

The HCPB was thermally treated at 1200 °C for 60 min under an argon flow in a tube furnace to realize carbonization after manual grinding. The resulting hard carbons were denoted as CHCPB (Scheme 1).



Scheme 1. Schematic diagram of the synthesis of CHCPB.

2.3. Structural Characterization

The composition structure of products was studied by Fourier transform-infrared (FTIR, Bruker, Bremen, Germany) spectra on a Bruker VERTEX 80v. Solid-state ¹³C CP/MAS NMR spectra were performed on a WB 600 MHz Bruker Avance III spectrometer (Bruker, Bremen, Germany). The surface areas were calculated from nitrogen adsorption data by Brunauer–Emmett–Teller (BET) analysis. Pore size distributions were calculated by DFT methods via the adsorption branch. The morphology of the products was investigated using scanning electron microscopy (SEM, JSM-7001F, Jeol, Tokyo, Japan) and transmission electron microscopy (TEM, JEM-2100F, Jeol, Tokyo, Japan). The structure of products was determined by X-ray diffraction (XRD, D8 ADVANCE A25, Bruker, Bremen, Germany) and Raman spectrometry (Horiba LabRAM HR Evolution, Horiba, Kyoto, Japan). The X-ray photoelectron spectroscopy (XPS, AXIS ULTRA DLD, Kratos, Manchester, UK) was used to study the surface chemical composition of obtained samples. The elemental analysis (EA) measurements were performed on a Vario EL CUBE elemental analyzer (Elementar, Frankfurt, Germany). The thickness and size of the nanosheets were obtained on a Bruker Dimension Icon atomic force microscope (AFM, Bruker, Bremen, Germany) in tapping mode.

2.4. Electrochemical Measurement

The electrochemical features of hard carbon materials were explored by assembling a CR2016 coin type cell in the glovebox. A 1 M amount of LiPF₆ in the mixed solvent of vinyl carbonate (EC) and diethyl carbonate (DEC) (1:1, vol/vol) with 5.0% fluoroethylene carbonate (FEC) was used as the electrolyte. Celgard 2400 membranes were used as the separator, and metal lithium slices acted as the counter electrode. The working electrode was made from a mixture of active materials, conductive carbon black, and polyvinylidene fluoride solution (2% PVDF) at the weight ratio of 6:3:1, with N-methylpyrrolidone (NMP) as the solvent. The obtained slurry was loaded onto the copper foil and dried at 80 °C overnight. After that, the whole copper foil was punched to the circular pole piece with the diameter of 10 mm, and the mass loading was obtained in the range of 0.45–0.57 mg cm⁻².

The galvanostatic charge and discharge measurements were carried on a LAND BT2000 battery system in the voltage range of 0.01–3 V. Electrochemical impedance spectroscopy (EIS) and cyclic voltammetry (CV) were tested on a 660 E electrochemical working station.

3. Results

3.1. The Structure and Morphology Characterization of the Materials

The yield of HCPs was ~90% owing to the presence of FeCl_3 catalyst. The Fourier transform infrared (FT-IR) spectroscopy of the HCPB is exhibited in Figure S1. Stretching vibrations at 2932 and 2828 cm^{-1} and bending vibrations at 1427 cm^{-1} of C–H, as well as skeleton vibration at 1616 and 1460 cm^{-1} of the benzene ring were observed. The small peak at 1140 cm^{-1} could be attributed to the C–O bonds of the methoxy groups derived from unreacted DMB. More detailed characterization of HCPB was observed by ^{13}C CP/MAS NMR spectroscopy (Figure S2). The resonance peaks at 124, 114, and 102 ppm belonged to the carbon in the benzene ring attached to the aromatic ring and non-substituted aromatic carbon, respectively. The resonance peaks at 55 and 153 ppm were ascribed to the unreacted methyl in the crosslinking agent and the aromatic carbon connected to the methoxy group. The above results indicated that DMB formed highly cross-linked networks with benzene rings as bridges [26].

The Raman spectra of the two samples are shown in Figure 1a. The peaks at 1190, 1435, and 1636 cm^{-1} were assigned to the stretching vibration of C–H in the plane and the vibration of aromatic rings and benzene rings, respectively. In addition, Raman peaks at 1337 and 1591 cm^{-1} were attributed to the D and G bands, which are typical spectral features of conjugated carbon frameworks [20,27]. After high temperature treatment, the spectrum of CHCPB exhibited only two typical D and G peaks, indicating the very stable conjugated skeleton. The ratio of the D-band (defect-induced mode) to the G-band (graphitic mode) denoted the degree of graphitization of material [28]. For CHCPB, the I_D/I_G value was 1.05, which suggested the existence of CHCPB defects. Both XPS and EA measurements revealed the presence of O elements in CHCPB (Figure S3 and Table S1). It was evident that the oxygen functional groups could not only increase the accessibility of electrode materials in electrolyte but also enhanced the storage capacity of Li^+ ions [29].

The N_2 adsorption–desorption isotherms were obtained to analyze the changes of the pore structure and specific surface area. Type I isotherms were found for the two samples. As shown in Figure 1c, they all had a sharp adsorption capacity at relatively low pressure. The adsorption almost reached saturation within a very small pressure variation range, indicating the microporous characteristic. The adsorption curve rose slowly in the pressure range of 0.3–1.0, and a clear hysteresis loop was observed. This indicated the presence of mesopores and few macropores in HCPB. However, the desorption curve did not cooperate with the adsorption curve in the low-pressure region, perhaps because the deformation of the polymer skeleton may have led to narrowed micropore pores, and the adsorbed molecules were unable to desorb completely. The pore size distributions of CHCPB and HCPB were mainly concentrated in 0.7 nm and 0.5–1.2 nm, respectively (Figure 1d), which was consistent with the above analysis. The specific surface area and pore structure parameters of the samples are summarized in Table 1. CHCPB had a similar specific surface area as HCPB. However, the micropore pore volume increased from 0.148 to 0.226 $\text{cm}^3 \text{g}^{-1}$, while the mesopore pore volume decreased from 0.197 to 0.070 $\text{cm}^3 \text{g}^{-1}$. The possible reason was the slight shrinkage of the skeleton of the material after carbonization, which increased the micropores and reduced the mesopores and macropores. Overall, the skeleton of CHCPB still maintained the original rigid skeleton.

X-ray diffraction (XRD) was used to investigate the phase structure of the materials (Figure 1b). It can be clearly seen that the curve of HCPB only showed a broad peak at 24°, indicating its amorphous nature. However, CHCPB had a sharp peak at 26° and a small peak at 42°, corresponding to the (002) and (100) planes of graphite [30], respectively, which suggested that the heat treatment strengthened the π – π conjugated and increased the order degree. CHCPB tended to form layer-stacking structures due to the strong interlayer π – π

interactions. Furthermore, two small peaks could be observed at 33.6° and 36.2° , which may have originated from traces of Fe_2O_3 formed by the residual catalyst.

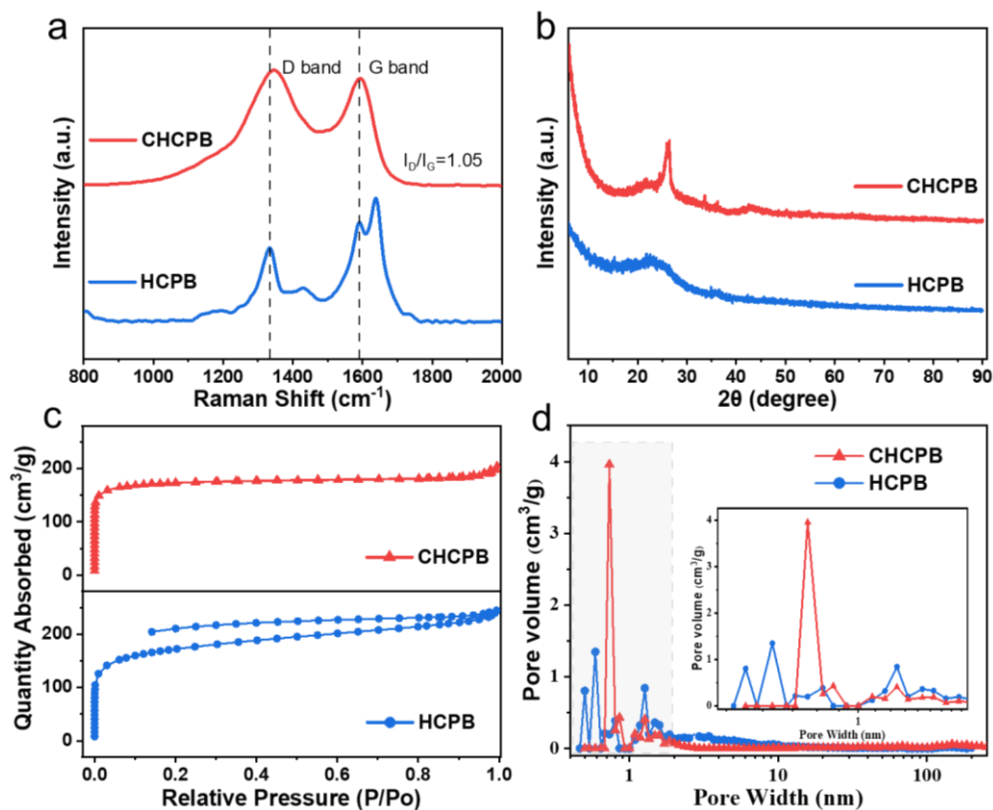


Figure 1. (a) Raman spectra and (b) XRD patterns of HCPB and CHCPB; (c) N_2 adsorption-desorption isothermal curves; and the pore size distribution curves (d) of HCPB and CHCPB.

Table 1. Porosity parameters of polymer and hard carbon.

| Sample | S_{BET} ($\text{m}^2 \text{g}^{-1}$) | V_{micro} ($\text{cm}^3 \text{g}^{-1}$) | V_{meso} ($\text{cm}^3 \text{g}^{-1}$) | V_{total} ($\text{cm}^3 \text{g}^{-1}$) |
|--------|---|--|---|--|
| HCPB | 593 | 0.15 | 0.20 | 0.38 |
| CHCPB | 583 | 0.23 | 0.07 | 0.32 |

The morphologies of materials were observed by SEM (Figure 2a,b). It could be seen that HCPB displayed a clear network structure. However, the CHCPB presented a layer-stacking structure, which was caused by strong π - π interactions among molecules. In addition, these two samples were also examined by TEM, and the disordered microcrystal structure of the CHCPB and HCPB could be distinctly observed (Figure 2c,d). The selected area electron diffraction (SAED) image of HCPB exhibited diffuse diffraction rings, further confirming the amorphous structure. On the contrary, CHCPB exhibited a partial short-range ordered graphite domain structure and sharper diffraction rings, which proved the microcrystal structure and layer-by-layer stacking nature.

To further prove the existence of the layered structure, CHCPB was stripped into a colloidal dispersion by the ultrasonic-assisted solvent exfoliation method, exhibiting a clear Tyndall effect. The AFM image further confirmed the precise information of CHCPB nanosheets (Figure 2e,f). The thickness of the nanosheets varied from 2 to 4 nm, which corresponded to the few-layered structure of CHCPB. Notably, the transverse dimensions of the nanosheets changed from 550 to 2200 nm, resulting in an aspect ratio of height and thus confirming their two-dimensional (2D) stratification characteristics, which was in agreement with the SEM and TEM results.

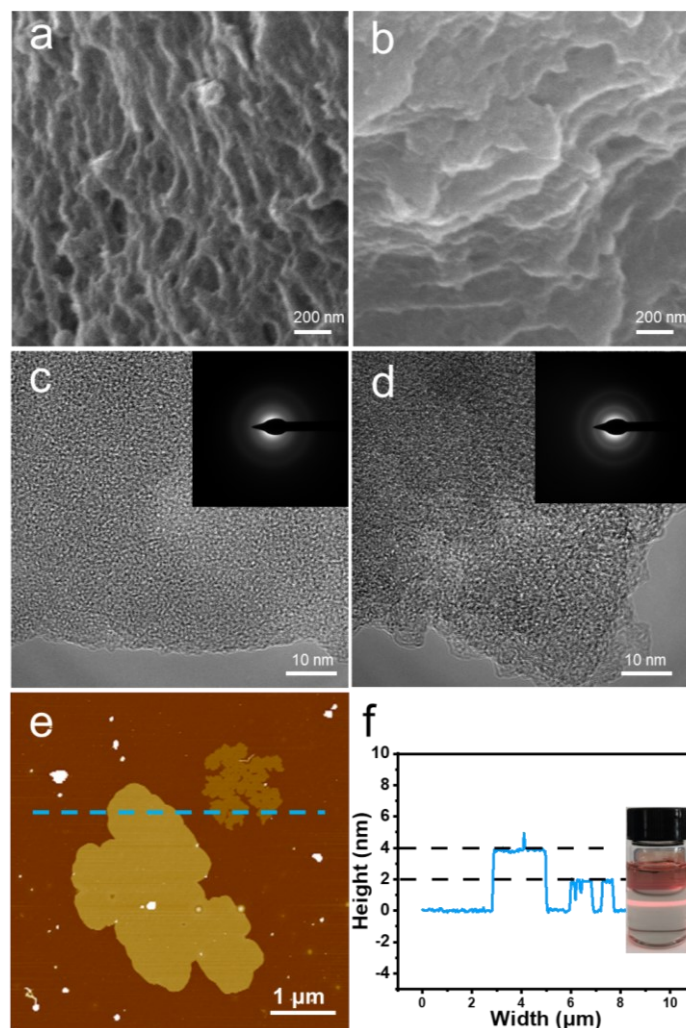


Figure 2. SEM images of (a) HCPB and (b) CHCPB; HRTEM images of (c) HCPB and (d) CHCPB; Inset: the SAED images; (e) AFM image of CHCPB nanosheet; (f) height profile along the line; Inset: optical image of CHCPB nanosheet in DMF solution.

3.2. Li Ion Storage Performances

Figure 3a,b show the CV curves of two electrode materials between 0.01 and 3 V at a scan rate of 0.1 mV s^{-1} . In the first anodic sweep, oxidation peaks appeared at 1.1 V, corresponding to the de-lithiation process of the HCPB electrode. From the first cycle, an oxidation peak at 1.9 V and a reduction peak at 1.7 V were formed, corresponding to the lithiation and de-lithiation of Li^+ within π -conjugated HCPB [27]. The anodic peak at 2.35 V was related to the process of forming CuO , and the copper probably derived from the current collector made of commercial copper foil [17,31]. For CHCPB, a broad peak at 1.15 V assigned to de-intercalation of Li^+ from the CHCPB electrode was also observed. Two obvious reduction peaks located at around 0.8 and 1.3 V during the first cathodic sweep sharply declined in the next two cycles, revealing the massive irreversible capacity loss ascribed to the development of solid electrolyte interphase (SEI) film on the electrode surface and other irreversible redox reactions between functional groups of HCPB/CHCPB with electrolyte [32]. The stable formation of SEI was beneficial to prevent further dissolution of electrolyte, thus enhancing the stabilization of the batteries [33]. The CV curves of the second and third circles were nearly overlapped in the subsequent cycles, which revealed the excellent redox activity of CHCPB [28]. Galvanostatic charge–discharge (GCD) tests of HCPB and CHCPB were further carried out at 0.1 A g^{-1} (Figure 3c,d). CHCPB delivered a higher initial charge/discharge capacity ($790.6/2260.8 \text{ mAh g}^{-1}$) than that

of HCPB ($474.4/2042.0 \text{ mAh g}^{-1}$). This may have been due to the defects and layered structure of CHCPB after high-temperature carbonization, which provided abundant storage sites for Li^+ ions [34]. A small platform close to 1.0 V at the first discharge curve was related to the formation of SEI film and the irreversible lithium-ion insertion reaction. The potential platform of discharge curves at around 1.0 V disappeared, and the charge–discharge curves hardly changed during the following cycles, suggesting that the CHCPB electrode was highly reversible.

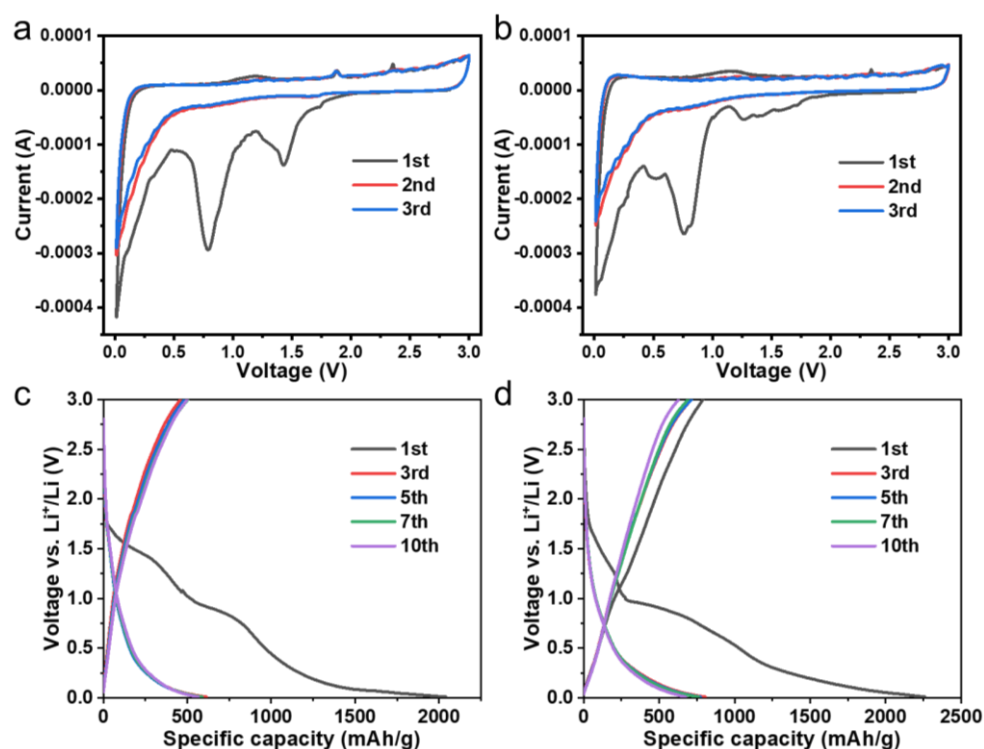


Figure 3. Cyclic voltammetry curves of (a) HCPB and (b) CHCPB at 0.1 mV s^{-1} ; GCD curves of (c) HCPB and (d) CHCPB at a current density of 0.1 A g^{-1} .

The presence of the π -conjugated structure allowed for the layer-by-layer arrangement of molecules, resulting in stable charged and discharged states, and enabling the CHCPB-based LIBs to achieve fast ionic transport, high-rate capability, and good cycling stability. The rate properties were measured at the current density of 0.1, 0.2, 0.3, 0.5, 1, and 2 A g^{-1} , respectively (Figure 4a). The discharge capacities of CHCPB were 699, 579, 527, 428, 338, and 261 mAh g^{-1} , respectively, much better than that of HCPB and most of the reported polymer-derived hard carbons (Table S2). Moreover, at the current density of 5 A g^{-1} , the discharge capacity of CHCPB was still as high as 165 mAh g^{-1} . When the current density recovered to 0.1 A g^{-1} , CHCPB reached a higher capacity (704 mAh g^{-1}) than that of its initial cycle, which was assigned to the activation of electrodes during the process of charging/discharging [20,28]. In stark contrast, the capacities of CHC only exhibited 246 mAh g^{-1} at 0.1 A g^{-1} and 121 mAh g^{-1} at 5 A g^{-1} (Figure S4). The excellent rate performance of the CHCPB electrode profited from the enhanced ionic conductivity of the stacked layered structure, which was of great significance for fast charging/discharging. Figure S5 presents the 1st, 2nd, 100th, 200th, 500th, 1000th, and 2000th GCD curves of HCPB and CHCPB at 2 A g^{-1} . The initial charge/discharge capacities were $331.7/1490.3 \text{ mAh g}^{-1}$ for CHCPB and $249.9/1461.1 \text{ mAh g}^{-1}$ for HCPB, and their coulombic efficiency (CE) values were 22.26% and 17.10%, respectively. The low CE may have resulted from the formation of the SEI layer [35]. Figure 4c displays the long-term cycling test results at 2 A g^{-1} . In the initial 50 cycles, the discharge capacity rapidly decreased, which may be owing to the continuous formation and decomposition of SEI film and the volume change

of electrodes during the Li^+ insertion and extraction [36]. At the 200th cycle, the cells achieved charge/discharge capacities that increased to $313.4/315.5 \text{ mAh g}^{-1}$ with a CE of 99.33% for CHCPB and $295.3/297.8 \text{ mAh g}^{-1}$ with a CE of 99.16% for HCPB, which were caused by electrode activation. The capacity of the two electrodes gradually decayed in the subsequent cycles, denoting that the electrode activation process was completed. The specific discharge capacity of CHCPB decreased more slowly and was maintained at 148.0 mAh g^{-1} after 2000 cycles, which was higher than that of HCPB (92.7 mAh g^{-1}) and CHC (63.0 mAh g^{-1}). The relatively stable cycling performance of CHCPB might be attributed to its rigid skeleton. The above results indicated that CHCPB could serve as a potential anode material for high performance LIBs.

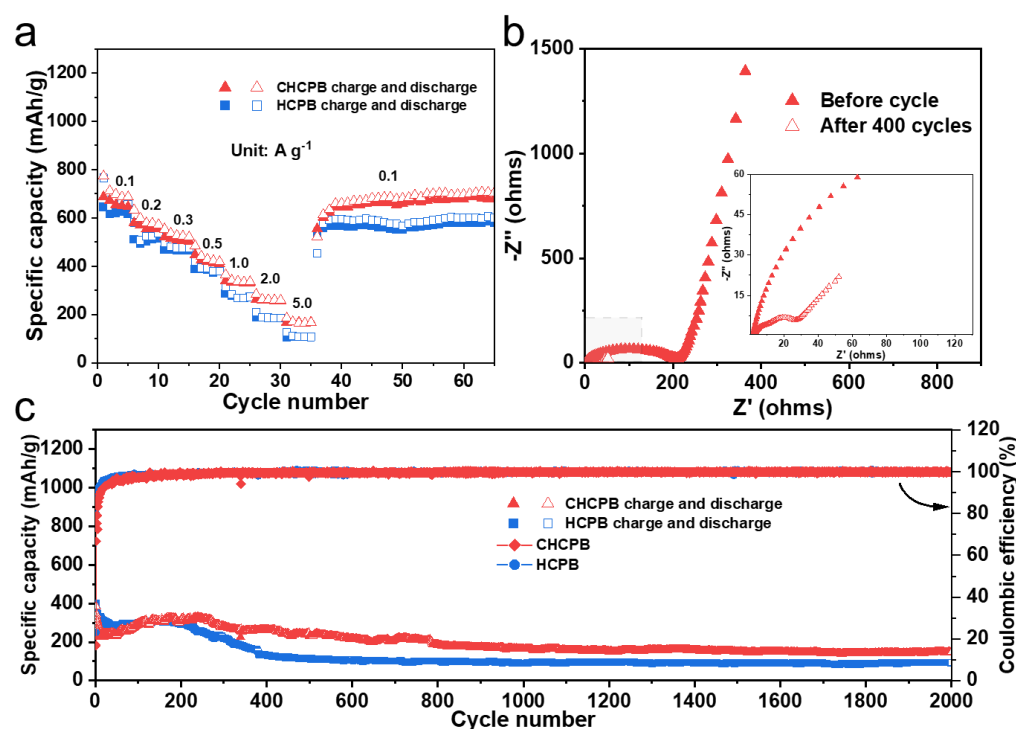


Figure 4. (a) Rate properties from 0.1 to 5 A g^{-1} and back to 0.1 A g^{-1} for HCPB and CHCPB; (b) EIS of CHCPB electrodes before and after the cycle; (c) long-term running properties of HCPB and CHCPB at 2 A g^{-1} .

Electrochemical impedance spectroscopy (EIS) was used to examine the interfacial properties of HCPB and CHCPB electrodes, and the fitting circuit model for the two electrodes can be found in Figure S6. The truncation of the Z_{real} axis in the high-frequency region belonged to the electrolyte resistance (R_s). The semi-circle at the high-frequency region referred to resistance of the SEI film (R_f). A semi-circle in the middle-frequency region was the charge transfer impedance (R_{ct}) between the electrode and electrolyte. The slope line in the low-frequency region was the Warburg impedance (Z_W) related to the diffusion of lithium ions in the electrode material [37]. As illustrated in Figure S7, the HCPB electrode showed 373Ω of the R_{ct} before the cycle. After the 400th cycle, a substantial increase in charge transport resistance was observed, which indicated the poor kinetic properties of charge carrier insertion/extraction. The above result can be ascribed to the presence of the network structure, whose crosslinked nodes blocked transmission channels, thus limiting the release of lithium ions. For the CHCPB electrode, the R_{ct} values before and after 400 cycles were 154 and 15Ω , respectively (Figure 4b), which were due to the formation of stable SEI film during charging and discharging. The data further demonstrated the higher electrical conductivity of CHCPB compared with HCPB. Moreover, the stable SEI film formed during cycling also decreased the interfacial resistance of the electrode, which was beneficial to the charge transfer and Li^+ transport.

The storage mechanism of the Li^+ ion was analyzed by testing the CV curves at different scan rates (Figure 5). The faster the scanning rate, the higher the peak current of the CV curve. The relationship between peak current (i) and sweep speed (v) was given by the following equation:

$$i = av^b \quad (1)$$

$$\log i = b \log v + \log a \quad (2)$$

where a and b are adjustable constants. When the b value approached 0.5, the storage process was diffusion-controlled (insertion/extraction). When the b value was close to 1.0, a capacitive process (surface adsorption/desorption behavior) dominated [38]. The calculated b value was 0.72 for HCPB and 0.85 for CHCPB, which meant that the lithium storage process in the two electrodes was primarily controlled by the capacitive process. The results verified that the surface capacitive behavior of the two electrodes dominates the storage capacity, being put down to the high specific surface area and the short ion diffusion distance [20].

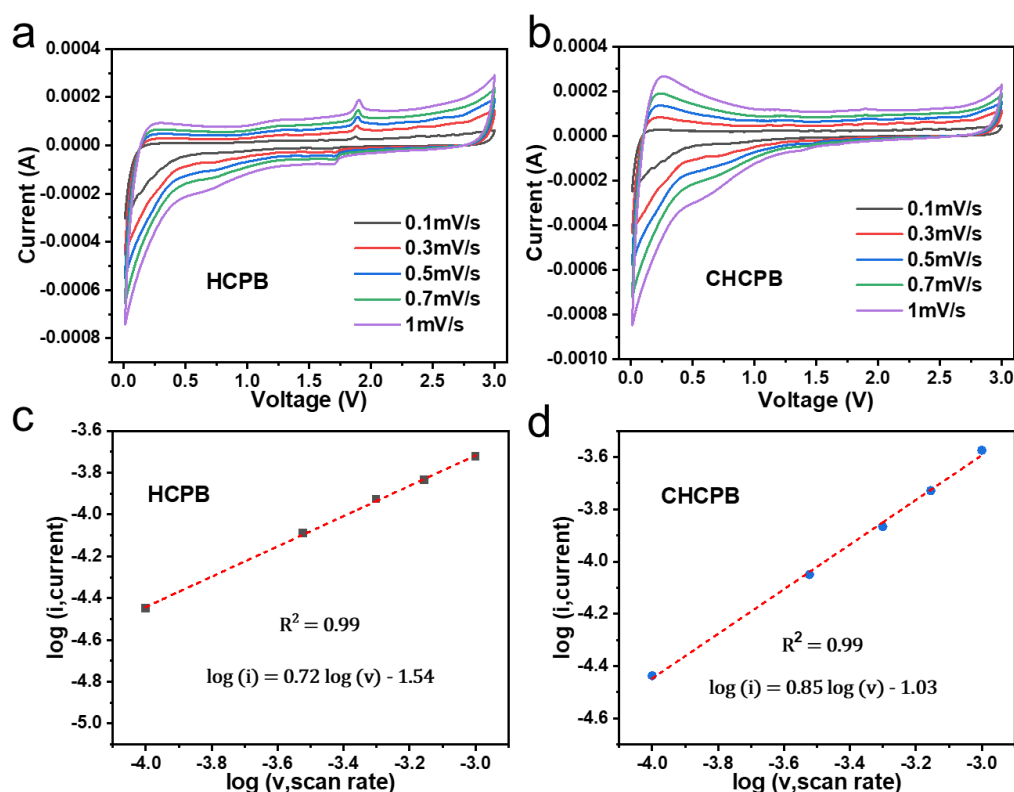


Figure 5. (a,b) CV curves of HCPB and CHCPB with scan rates from 0.1 to 1.0 mV s^{-1} ; (c,d) $\log(i)$ - $\log(v)$ graphs of HCPB and CHCPB.

The superior electrochemical properties of the CHCPB electrode could be attributed to its unique characteristics: (1) the high-temperature heat treatment and its π -conjugated structure enhanced the conductivity and promoted the electron transport; (2) the abundant micropores of the CHCPB electrode provided high specific surface area and a number of defects, thus providing abundant storage sites for lithium ions and improved capacity; (3) the stacked layered structure afforded fast channels for ion transport and thus better rate performance. In addition, the rigid backbone knitted by the aromatic structural units led to good cycling stability at high current densities of CHCPB.

4. Conclusions

In this work, the synthetic HCPB was carbonized at 1200 °C under argon atmosphere to obtain a hard carbon material (CHCPB). The layered structure of CHCPB improved

the stability and enriched the storage sites for Li^+ ions. The CHCPB electrode had a high reversible capacity of 699 mAh g^{-1} at 0.1 A g^{-1} . At the same time, the CHCPB electrode also showed a great rate of performance. The capacities were 699, 579, 527, 428, 338, 261, 165 and 704 mAh g^{-1} at 0.1, 0.2, 0.3, 0.5, 1.0, 2.0, 5.0, and 0.1 A g^{-1} , respectively for Li | | CHCPB batteries. The CHCPB electrode displayed outstanding electrochemical performance because of the larger specific surface area, more defects, faster ion transport, and a more stable structure. Based on this study, we can also endow the precursors with different pore structures and functionalized crosslinking networks through a flexible molecular design to meet different application requirements.

Supplementary Materials: The following supporting information can be downloaded at: <https://www.mdpi.com/article/10.3390/coatings13020421/s1>, Figure S1: FTIR spectra of HCPB; Figure S2: ^{13}C CP/MAS NMR spectra of HCPB; Figure S3: The XPS spectrum of CHCPB; Figure S4: (a) The rate property and (b) long-term running property at 2 A g^{-1} of commercial hard carbon (CHC); Figure S5: Galvanostatic charge–discharge curves of (a) HCPB and (b) CHCPB at 2 A g^{-1} . Figure S6: The EIS fitting circuit model of HCPB and CHCPB electrodes; Figure S7: EIS of the HCPB electrode before (a) and after cycling (b); Table S1. The elemental composition determined by EA. Table S2. Comparison of the electrochemical performances with some reported polymers-derived carbon materials.

Author Contributions: Investigation, Z.G.; writing—original draft preparation, Z.G.; writing—review and editing, Y.S., X.T. and T.Y.; supervision, Y.S. and C.W.; conceptualization, X.T. and T.Y.; formal analysis, Z.M. and X.G.; project administration, Y.S.; funding acquisition, Y.S., X.T. and T.Y. All authors have read and agreed to the published version of the manuscript.

Funding: This work was supported by the National Natural Science Foundation of China (Nos. 52072383, U21A2061, and No. 22209197), Natural Science Foundation of Shanxi Province (202203021211002), Shanxi Province Science Foundation for Youths (No. SQ2019001), and the Innovation Fund of Institute of Coal Chemistry, Chinese Academy of Sciences (No. SCJC-XCL-2022-08).

Institutional Review Board Statement: Not applicable.

Informed Consent Statement: Not applicable.

Data Availability Statement: All data that support the findings of this study are included within the article.

Conflicts of Interest: The authors declare no conflict of interest.

References

1. Zhang, H.; Liu, Q.; Fang, Y.; Teng, C.; Liu, X.; Fang, P.; Tong, Y.; Lu, X. Boosting Zn-Ion Energy Storage Capability of Hierarchically Porous Carbon by Promoting Chemical Adsorption. *Adv. Mater.* **2019**, *31*, 1904948. [CrossRef]
2. Zhang, C.; Ma, Y.; Zhang, X.; Abdolhosseinzadeh, S.; Sheng, H.; Lan, W.; Pakdel, A.; Heier, J.; Nüesch, F. Two-Dimensional Transition Metal Carbides and Nitrides (MXenes): Synthesis, Properties, and Electrochemical Energy Storage Applications. *Energy Environ. Mater.* **2020**, *3*, 29–55. [CrossRef]
3. Lu, Y.; Wang, J.; Zeng, S.; Zhou, L.; Xu, W.; Zheng, D.; Liu, J.; Zeng, Y.; Lu, X. An ultrathin defect-rich Co_3O_4 nanosheet cathode for high-energy and durable aqueous zinc ion batteries. *J. Mater. Chem. A* **2019**, *7*, 21678–21683. [CrossRef]
4. Zhang, C.; Park, S.-H.; O'Brien, S.E.; Seral-Ascaso, A.; Liang, M.; Hanlon, D.; Krishnan, D.; Crossley, A.; McEvoy, N.; Coleman, J.N.; et al. Liquid exfoliation of interlayer spacing-tunable 2D vanadium oxide nanosheets: High capacity and rate handling Li-ion battery cathodes. *Nano Energy* **2017**, *39*, 151–161. [CrossRef]
5. Tang, H.; Li, W.; Pan, L.; Cullen, C.P.; Liu, Y.; Pakdel, A.; Long, D.; Yang, J.; McEvoy, N.; Duesberg, G.S.; et al. In Situ Formed Protective Barrier Enabled by Sulfur@Titanium Carbide (MXene) Ink for Achieving High-Capacity, Long Lifetime Li-S Batteries. *Adv. Sci.* **2018**, *5*, 1800502. [CrossRef]
6. Abdolhosseinzadeh, S.; Schneider, R.; Verma, A.; Heier, J.; Nüesch, F.; Zhang, C. Turning Trash into Treasure: Additive Free MXene Sediment Inks for Screen-Printed Micro-Supercapacitors. *Adv. Mater.* **2020**, *32*, 2000716. [CrossRef]
7. Zhao, L.-F.; Hu, Z.; Lai, W.-H.; Tao, Y.; Peng, J.; Miao, Z.-C.; Wang, Y.-X.; Chou, S.-L.; Liu, H.-K.; Dou, S.-X. Hard Carbon Anodes: Fundamental Understanding and Commercial Perspectives for Na-Ion Batteries beyond Li-Ion and K-Ion Counterparts. *Adv. Energy Mater.* **2021**, *11*, 2002704. [CrossRef]
8. Zhang, X.; Yang, Y.; Zhou, Z. Towards practical lithium-metal anodes. *Chem. Soc. Rev.* **2020**, *49*, 3040–3071. [CrossRef]

9. Dahbi, M.; Kiso, M.; Kubota, K.; Horiba, T.; Chafik, T.; Hida, K.; Matsuyama, T.; Komaba, S. Synthesis of hard carbon from argan shells for Na-ion batteries. *J. Mater. Chem. A* **2017**, *5*, 9917–9928. [[CrossRef](#)]
10. Long, W.; Fang, B.; Ignaszak, A.; Wu, Z.; Wang, Y.-J.; Wilkinson, D. Biomass-derived nanostructured carbons and their composites as anode materials for lithium ion batteries. *Chem. Soc. Rev.* **2017**, *46*, 7176–7190. [[CrossRef](#)] [[PubMed](#)]
11. Beda, A.; Taberna, P.-L.; Simon, P.; Matei Ghimbeu, C. Hard carbons derived from green phenolic resins for Na-ion batteries. *Carbon* **2018**, *139*, 248–257. [[CrossRef](#)]
12. Saurel, D.; Orayech, B.; Xiao, B.; Carriazo, D.; Li, X.; Rojo, T. From Charge Storage Mechanism to Performance: A Roadmap toward High Specific Energy Sodium-Ion Batteries through Carbon Anode Optimization. *Adv. Energy Mater.* **2018**, *8*, 1703268. [[CrossRef](#)]
13. Fujimoto, H.; Tokumitsu, K.; Mabuchi, A.; Chinnasamy, N.; Kasuh, T. The anode performance of the hard carbon for the lithium ion battery derived from the oxygen-containing aromatic precursors. *J. Power Sources* **2010**, *195*, 7452–7456. [[CrossRef](#)]
14. Fromm, O.; Heckmann, A.; Rodehorst, U.C.; Frerichs, J.; Becker, D.; Winter, M.; Placke, T. Carbons from biomass precursors as anode materials for lithium ion batteries: New insights into carbonization and graphitization behavior and into their correlation to electrochemical performance. *Carbon* **2018**, *128*, 147–163. [[CrossRef](#)]
15. Ni, J.; Huang, Y.; Gao, L. A high-performance hard carbon for Li-ion batteries and supercapacitors application. *J. Power Sources* **2013**, *223*, 306–311. [[CrossRef](#)]
16. Xu, S.; Luo, Y.; Tan, B. Recent Development of Hypercrosslinked Microporous Organic Polymers. *Macromol. Rapid Commun.* **2013**, *34*, 471–484. [[CrossRef](#)]
17. Zhang, Q.; Dai, Q.; Yan, C.; Su, C.; Li, A. Nitrogen-doped porous carbon nanoparticle derived from nitrogen containing conjugated microporous polymer as high performance lithium battery anode. *J. Alloys Compd.* **2017**, *714*, 204–212. [[CrossRef](#)]
18. Yang, X.; Wei, C.; Sun, C.; Li, X.; Chen, Y. High performance anode of lithium-ion batteries derived from an advanced carbonaceous porous network. *J. Alloys Compd.* **2017**, *693*, 777–781. [[CrossRef](#)]
19. Zhang, C.; Kong, R.; Wang, X.; Xu, Y.; Wang, F.; Ren, W.; Wang, Y.; Su, F.; Jiang, J.-X. Porous carbons derived from hypercrosslinked porous polymers for gas adsorption and energy storage. *Carbon* **2017**, *114*, 608–618. [[CrossRef](#)]
20. Li, C.; Kong, D.; Wang, B.; Du, H.; Zhao, J.; Dong, Y.; Xie, Y. Conjugated microporous polymer derived N, O and S co-doped sheet-like carbon materials as anode materials for high-performance lithium-ion batteries. *J. Taiwan Inst. Chem. Eng.* **2022**, *134*, 104293. [[CrossRef](#)]
21. Zhang, Q.; Xu, Z.; Bai, Y.; Zhang, Y. Low temperature synthesis and superior lithium storage properties of fluorine-rich tubular porous carbon. *J. Alloys Compd.* **2022**, *901*, 163657. [[CrossRef](#)]
22. Zhang, Q.; Zhang, Y.; Lian, F.; Xu, Z.; Wang, X. Synthesis and lithium storage properties of nitrogen-containing hard carbon from conjugated microporous polymers. *Ionics* **2022**, *28*, 2623–2633. [[CrossRef](#)]
23. Wang, X.; Mu, P.; Zhang, C.; Chen, Y.; Zeng, J.; Wang, F.; Jiang, J.X. Control Synthesis of Tubular Hyper-Cross-Linked Polymers for Highly Porous Carbon Nanotubes. *ACS Appl. Mater. Interfaces* **2017**, *9*, 20779–20786. [[CrossRef](#)] [[PubMed](#)]
24. Guan, T.; Zhao, J.; Zhang, G.; Wang, J.; Zhang, D.; Li, K. Template-Free Synthesis of Honeycomblike Porous Carbon Rich in Specific 2–5 nm Mesopores from a Pitch-Based Polymer for a High-Performance Supercapacitor. *ACS Sustain. Chem. Eng.* **2018**, *7*, 2116–2126. [[CrossRef](#)]
25. Xu, F.; Han, H.; Qiu, Y.; Zhang, E.; Repich, H.; Qu, C.; Yu, H.; Wang, H.; Kaskel, S. Facile regulation of carbon framework from the microporous to low-porous via molecular crosslinker design and enhanced Na storage. *Carbon* **2020**, *167*, 896–905. [[CrossRef](#)]
26. Wang, S.; Zhang, C.; Shu, Y.; Jiang, S.; Xia, Q.; Chen, L.; Jin, S.; Hussain, I.; Cooper, A.I.; Tan, B. Layered microporous polymers by solvent knitting method. *Sci. Adv.* **2017**, *3*, e1602610. [[CrossRef](#)] [[PubMed](#)]
27. Ye, X.-L.; Huang, Y.-Q.; Tang, X.-Y.; Xu, J.; Peng, C.; Tan, Y.-Z. Two-dimensional extended π -conjugated triphenylene-core covalent organic polymer. *J. Mater. Chem. A* **2019**, *7*, 3066–3071. [[CrossRef](#)]
28. Li, C.; Guo, X.; Du, H.; Zhao, J.; Liu, L.; Yuan, Q.; Fu, C. The synthesis of the D-A-type polymers containing benzo[1,2-b:6,5-b']dithiophene-4,5-dione unit, their composites with carbon, and the lithium storage performances as electrode materials. *J. Solid State Electrochem.* **2021**, *25*, 1847–1859. [[CrossRef](#)]
29. Piedboeuf, M.-L.C.; Job, N.; Aqil, A.; Busby, Y.; Fierro, V.; Celzard, A.; Detrembleur, C.; Léonard, A.F. Understanding the Influence of Surface Oxygen Groups on the Electrochemical Behavior of Porous Carbons as Anodes for Lithium-Ion Batteries. *ACS Appl. Mater. Interfaces* **2020**, *12*, 36054–36065. [[CrossRef](#)]
30. Ni, B.; Li, Y.; Chen, T.; Lu, T.; Pan, L. Covalent organic frameworks converted N, B co-doped carbon spheres with excellent lithium ion storage performance at high current density. *J. Colloid Interface Sci.* **2019**, *542*, 213–221. [[CrossRef](#)] [[PubMed](#)]
31. Mao, Y.; Duan, H.; Xu, B.; Zhang, L.; Hu, Y.; Zhao, C.; Wang, Z.; Chen, L.; Yang, Y. Lithium storage in nitrogen-rich mesoporous carbon materials. *Energy Environ. Sci.* **2012**, *5*, 7950–7955. [[CrossRef](#)]
32. Yang, Y.; Yuan, J.; Huang, S.; Chen, Z.; Lu, C.; Yang, C.; Zhai, G.; Zhu, J.; Zhuang, X. Porphyrinic conjugated microporous polymer anode for Li-ion batteries. *J. Power Sources* **2022**, *531*, 231340. [[CrossRef](#)]
33. Yang, L.; Wei, W.; Ma, Y.; Xu, Y.; Chang, G. Intermolecular channel expansion induced by cation- π interactions to enhance lithium storage in a crosslinked π -conjugated organic anode. *J. Power Sources* **2020**, *449*, 227551. [[CrossRef](#)]
34. Zhang, Y.; Li, J.; Gong, Z.; Xie, J.; Lu, T.; Pan, L. Nitrogen and sulfur co-doped vanadium carbide MXene for highly reversible lithium-ion storage. *J. Colloid Interface Sci.* **2021**, *587*, 489–498. [[CrossRef](#)] [[PubMed](#)]

35. Song, Z.; Zhou, H. Towards sustainable and versatile energy storage devices: An overview of organic electrode materials. *Energy Environ. Sci.* **2013**, *6*, 2280–2301. [[CrossRef](#)]
36. Liu, N.; Lu, Z.; Zhao, J.; McDowell, M.T.; Lee, H.-W.; Zhao, W.; Cui, Y. A pomegranate-inspired nanoscale design for large-volume-change lithium battery anodes. *Nat. Nanotechnol.* **2014**, *9*, 187–192. [[CrossRef](#)] [[PubMed](#)]
37. Li, Z.; Zhong, W.; Cheng, A.; Li, Z.; Li, L.; Zhang, H. Novel hyper-crosslinked polymer anode for lithium-ion batteries with highly reversible capacity and long cycling stability. *Electrochim. Acta* **2018**, *281*, 162–169. [[CrossRef](#)]
38. Jiang, G.; Qiu, Y.; Lu, Q.; Zhuang, W.; Xu, X.; Kaskel, S.; Xu, F.; Wang, H. Mesoporous Thin-Wall Molybdenum Nitride for Fast and Stable Na/Li Storage. *ACS Appl. Mater. Interfaces* **2019**, *11*, 41188–41195. [[CrossRef](#)]

Disclaimer/Publisher's Note: The statements, opinions and data contained in all publications are solely those of the individual author(s) and contributor(s) and not of MDPI and/or the editor(s). MDPI and/or the editor(s) disclaim responsibility for any injury to people or property resulting from any ideas, methods, instructions or products referred to in the content.